



Grave-to-cradle upcycling of harmful algal biomass into atomically dispersed iron catalyst for efficient ammonia electrosynthesis from nitrate

He Wang ^{a,1}, Shuaishuai Man ^{b,1}, Han Wang ^{a,c}, Volker Presser ^{d,e,f}, Qun Yan ^{a,c,g,*}, Yong Zhang ^h

^a School of Environmental and Civil Engineering, Jiangnan University, Wuxi 214122, PR China

^b College of Chemistry and Chemical Engineering, Chongqing University, Chongqing 401331, PR China

^c Jiangsu Key Laboratory of Anaerobic Biotechnology, Wuxi 214122, PR China

^d INM, Leibniz Institute for New Materials, Campus D2.2, 66123 Saarbrücken, Germany

^e Department for Materials Science and Engineering, Saarland University, Campus D2.2, 66123 Saarbrücken, Germany

^f Saarene, Saarland Center for Energy Materials and Sustainability, Campus C4.2, 66123 Saarbrücken, Germany

^g Jiangsu Collaborative Innovation Center of Technology and Material of Water Treatment, Suzhou 215011, PR China

^h Jiangsu Hongqi Biotechnology Co. Ltd, Taizhou 225316, PR China



ARTICLE INFO

Keywords:

Electrochemical nitrate reduction

HABs resource utilization

Single-atom catalyst

Ammonia recovery

Biochar

ABSTRACT

Electrochemically converting nitrate, widely distributed in industrial wastewater and contaminated water bodies, into ammonia is a promising route for resource recovery and wastewater treatment. Meanwhile, treating harmful algal blooms (HABs) is presented worldwide, are time and resource-consuming, and carries a high CO₂ footprint. Rather than considering this carbon and nitrogen-rich biomass as disposable waste, consider it a vast renewable resource. Therefore, this study presents a Fe-dispersed carbon-based catalyst derived from HABs biomass, with a maximum ammonia yield rate of 16449 µg h⁻¹ cm⁻² (1.2 mmol h⁻¹ mg_{cat}⁻¹) and NH₃ Faradaic efficiency of 87.3%. This catalyst also possessed decent stability with continuous operation over 50 h. Experimental and theoretical calculation results reveal that the Fe-N₄ site facilitates electrocatalytic nitrate reduction reaction by reducing the energy barriers of the NO₃-to-NH₃ pathway. Thus, this strategy of upcycling HABs biomass waste into functional catalysts offers a multipronged approach to renewable and carbon-neutral energy technologies.

1. Introduction

Algal biomass harvested from harmful algal blooms (HABs) exceeded two million tons per year in Taihu Lake, Jiangsu Province of China [1]. Together with phosphate, nitrate and ammonia are major class pollutants within a eutrophicated waterbody, which are all responsible for algal blooming [2]. However, conventional HABs treatments, including flocculants addition for collecting, dewatering for volume reduction, and mixed combustion or bio-methanation for power generation, all bring about larger CO₂ footprints [3,4]. Different from conventional biological or physio-chemical removal that eventually converts all nitrogen pollutants into dinitrogen gas, upcycling nitrate resource into ammonia (NH₃) would be more attractive in light of the low-carbon prospects against climate change [5–7]. Rather than being adopted for fertilizers synthesis, NH₃ is recently regarded as a potential renewable hydrogen energy vector or energy fuel [8–11]. Instead of the currently

energy-intensive Haber-Bosch process, sustainable ammonia production approaches are encouraged to help alleviate the looming greenhouse effect [12,13]. Herein, converting nitrate pollutants into ammonia might contribute more to the water-HABs-fertilizer-energy nexus regarding nitrogen cycling.

Compared to the electrochemical methods for decentralized NH₃ synthesis using N₂ reduction reaction (NRR) at ambient conditions [5, 13–15], electrocatalytic nitrate reduction (NO₃RR) has been widely considered as a viable approach to recover nitrogen owing to the relatively low dissociation energy (N = O, 204 kJ mol⁻¹), and the favorable kinetics [5,10,16]. Various catalysts, including metals [17], metal composites [18], heteroatom-doped carbon [19], and even biological enzymes [20], have been explored to achieve high performance and selectivity for NO₃RR. Amongst, metal-doped carbon-based catalysts are more attractive for practical application due to the merits of competitive performance as noble metal catalysts and low cost [6,21]. In nature,

* Corresponding author at: School of Environmental and Civil Engineering, Jiangnan University, Wuxi 214122, PR China.

E-mail address: yanqun@jiangnan.edu.cn (Q. Yan).

¹ He Wang and Shuaishuai Man contributed equally.

nitrate and nitrite reductase is an enzyme that catalyzes the reduction of NO_3^- to $\text{NH}_3/\text{NH}_4^+$, of which Fe protein plays an important role in the enzymatic cascades [20]. Therefore, Fe-doped carbon material has become a promising catalyst that can be used for electrochemical NO_3RR due to its unique advantages, such as cheap and easy to obtain, low-toxic and harmless, and excellent catalytic performance [15]. Although widely adopted as carbon precursors, metal-organic framework (MOFs) and organic polymeric, exhibit structural tunability and appealing NO_3RR performance [2,6,22–24], they have high costs and potential environmental risks [25–29]. Consequently, using economical biomass as a carbon-based catalyst precursor for NO_3RR might be promising for NH_3 green fabrication [30,31]. To develop biochar-based electrocatalysts for NO_3RR , a few concerns are to be addressed, such as the (1) lack of enough active sites leading to poor Faradaic efficiency (FE) and ammonia selectivity [32], (2) to achieve both industrial-relevant current densities ($>100 \text{ mA cm}^{-2}$) and high ammonia FE [31], and (3) possess large overpotential and insufficient stability [33]. To tackle the above-mentioned challenges, the single atom catalysts (SACs) appear to be an ideal choice as they can greatly increase metal utilization thereby accelerating catalytic activity and reducing metal loss during catalysis [34]. It has been demonstrated that the biomass derived carbon-based Fe SACs could promote the oxygen reduction reaction (ORR) and advanced oxidation processes (AOPs) [35, 36]. However, studies on Fe SACs that are derived from biomass and used for NO_3RR have been rarely reported. NO_3RR performance can also be improved by introducing nitrogen doping in the biochar matrix [32]. Thus, as a typical nitrogen-rich precursor leading to nitrogen self-doping [37–39], algal biomass-derived nitrogen dopants could not only serve as active sites but as anchor sites to immobilize iron atoms and formed into Fe, N co-doped biochar SACs (Fe-N-BC SACs) [40]. Therefore, upcycling algal biomass wastes from HABs to prepare Fe-N-BC SACs for NO_3RR might be promising.

In this study, abundant and zero-cost HABs biomass was implemented as carbon precursor to prepare NO_3RR electrocatalysts for efficient ammonia generation under different nitrate concentrations. A strategy of increasing the catalytic site density was employed to overcome low current density and kinetic sluggishness in NO_3RR . With the assistance of intrinsic nitrogen from algal biomass, Fe single-atom confinement was realized. The atomic site for Fe and the chemical coordination as FeN_4 were identified by aberration-corrected high-angle annular dark field scanning transmission electron microscopy (HAADF-STEM), X-ray photoelectron spectroscopy (XPS), and X-ray absorption fine-structure (XAFS). Density functional theory (DFT) calculations also revealed the positive effect of highly dispersed Fe active sites, which accounts for the high nitrate-to-ammonia performance. C-N coupling was also achieved in this electrochemical system for urea synthesis in the cathode compartment after CO_2 was supplied. This research demonstrated the feasibility of NO_3RR by using algal biomass waste-derived electrocatalysts and shed new light on carbon neutrality.

2. Experimental

2.1. Catalyst synthesis

After being oven-dried, 5 g of collected algal biomass was mixed with 200 mg iron acetylacetone (Fe-ac) and 2.5 g KOH, and was then finely ground in an agate mortar. Next, the powder was pyrolyzed under flowing Ar for 2 h at 800 °C with a heating rate of 5 °C min⁻¹. After being cooled down to room temperature and washed with 1 M HCl, ethanol, and deionized water several times, respectively, the collected sample was dried at 60 °C under vacuum and sieved through a 400-mesh screen. This iron atom dispersed carbon-based catalyst was named Fe-N-BC. Similarly, different transition metal doped carbon-based catalysts were synthesized (Co-N-BC and Cu-N-BC), except that using 200 mg cobalt acetylacetone (Co-ac) and cupric acetylacetone (Cu-ac) instead of Fe-ac. Besides, Fe-N-BC samples with different Fe doping levels were

synthesized using iron acetylacetone of 50 mg, 400 mg, and 600 mg. Also, the algal biomass mixed with KOH was pyrolyzed in the same procedures to obtain the N-BC. In addition, using commercially available graphite powders as a control named C.

2.2. Physicochemical characterization

The scanning electron microscope (SEM) observations were performed on a Hitachi SU8100 SEM. HAADF-STEM images were investigated by Themis Z (FEI) equipped with energy-dispersive X-ray diffraction (EDS) mapping at an accelerating voltage of 200 kV. X-ray diffraction (XRD) patterns were performed using a Bruker D2 PHASER X-ray diffractometer with a 2θ angle of 10–80°. Each sample was spread on the recess of XRD sample holder as a thin layer, and a diffraction pattern of a polysilicon wafers was measured to determine the instrumental broadening. Raman spectra were recorded using a LabRAM HR Evolution Raman spectrometer (Horiba) with an incident wavelength of 514 nm and a laser power of 0.5 mW. Samples for Raman spectroscopy were placed on a quartz slide and flattened. The Raman emission was collected by X 50 objective lens (numeric aperture is 0.75).

The XPS data were measured on a Thermo Scientific K-Alpha spectrometer, and the XPS spectra were calibrated by shifting the detected carbon C 1 s peak to 284.8 eV. Elemental analysis was performed on an Agilent 5110 ICP-OES spectrometer. XAFS measurements for the Fe K-edge were performed in fluorescence mode in Australia's Nuclear Science and Technology Organisation (ANSTO), Australia. The data processing for X-ray absorption near-edge spectroscopy (XANES) and X-ray absorption fine-structure spectroscopy (EXAFS) was performed using the ATHENA and ARTEMIS programs [41].

2.3. Electrochemical measurement

All the electrochemical measurements were carried out using a CHI 604E electrochemical workstation (Chenhua) in an H-type cell separated by a Nafion 117 proton exchange membrane (DuPont). The cathode and anode chamber of the H cell contained 50 mL of aqueous 1 M KOH with various concentrations of $\text{NO}_3\text{-N}$ (100, 700, 1400 $\mu\text{g mL}^{-1}$) as electrolytes, with the pH adjusted to 13.9. A platinum mesh and a mercuric oxide electrode (Hg/HgO) were used as the counter and reference electrodes, respectively. In this work, all the potentials measured against Hg/HgO electrode were converted to the reversible hydrogen electrode (RHE) scale as follows: $E(\text{vs.RHE}) = E(\text{vs.Hg/HgO electrode}) + 0.098\text{V} + 0.0591 \times \text{pH}$. The Ohmic resistance in the solution was determined using electrochemical impedance spectroscopy, and the measured potentials were 60% iR-compensated unless otherwise specified. The working electrode was prepared by drop-casting. In brief, 8 mg of catalyst and 50 μL Nafion (5%) were dispersed in 950 μL isopropanol and sonicated for 1 h to obtain a well-dispersed catalyst ink. Then, 100 μL of the catalyst ink was drop-cast on 1 × 1 cm² carbon paper (Toray, Japan) and dried at 50 °C in a vacuum oven for 12 h.

Before the electrochemical test, cyclic voltammetry (CV) curves are performed until the curves achieve steady-state ones at a rate of 50 mV s⁻¹ from 0.9 to –0.6 V. Linear sweep voltammetry (LSV) was carried out at a scan rate of 10 mV s⁻¹. Then, the potentiostat test was performed at different potentials for 4 h with a stirring rate of 700 rpm unless otherwise stated. The CV curves were recorded within a potential range of 0.1 V around open-circuit potential (OCP) to avoid apparent faradaic processes with a scan rate (v) of 5–60 mV s⁻¹. Then, the C_{dl} was calculated by:

$$C_{dl} = I_{capacitive} / v \quad (1)$$

The electrochemically active surface area (ECSA) was determined by:

$$\text{ECSA} = C_{dl} / C_s \quad (2)$$

where C_{dl} is the double layer capacitance and C_s is the specific capacitance of a typical value (0.04 mF cm^{-2} in 1 M KOH) [42].

2.4. Energy efficiency evaluate of NO_3RR and ammonia production

The nitrate removal efficiency was calculated as follows:

$$\text{Conversion} = \Delta C_{\text{NO}_3^- - N} / C_0 \times 100\% \quad (3)$$

where $\Delta C_{\text{NO}_3^-}$ is the concentration difference of NO_3^- -N before and after electrolysis, C_0 is the initial concentration of NO_3^- -N ($\mu\text{g mL}^{-1}$).

The selectivity of ammonia and nitrite was obtained by:

$$\text{Selectivity} = C / \Delta C_{\text{NO}_3^- - N} \times 100\% \quad (4)$$

where C is the generated concentration of ammonia or nitrite ($\mu\text{g mL}^{-1}$).

The ammonia yield rate was calculated by:

$$\text{Yield}_{\text{NH}_3} = C_{\text{NH}_3} \times V / t \times S \quad (5)$$

where C_{NH_3} is the concentration of ammonia after electrolysis ($\mu\text{g mL}^{-1}$), V is the catholyte volume (mL), t is the electrolysis time (h), and S is the geometric area of the working electrode (1 cm^2).

The Faradaic efficiency (FE) of NO_3RR towards NH_3 and H_2 were calculated as:

$$\text{FE}_{\text{NH}_3} = (8 \times V \times C_{\text{NH}_3} \times F) \times 100\% / Q \quad (6)$$

$$\text{FE}_{\text{H}_2} = (2 \times N_{\text{H}_2} \times F) \times 100\% / Q \quad (7)$$

where 8 is the number of electron transfers toward the formation of NH_3 , 2 is the number of electron transfers toward the formation of H_2 , N_{H_2} is the H_2 amount (mol), the generated H_2 was detected using a gas chromatograph (GC-9790, Fuli) with a thermal conductivity detector (TCD), F is the Faraday constant ($96,485 \text{ C mol}^{-1}$). Q is the total charge (C) passing the electrode, which was calculated based on integrating the $i-t$ curves.

The partial current density toward ammonia production (j_{NH_3} ; mA cm^{-2}) is the product of FE_{NH_3} and the applied current density (j_{Total} ; mA cm^{-2}):

$$j_{\text{NH}_3} = \text{FE} \times j_{\text{Total}} \quad (8)$$

The energy consumption (EC) for ammonia electrosynthesis (kWh kg^{-1}) was calculated according to the equation:

$$\text{EC} = E_{\text{cell}} \times I \times t / 1000 \times m \quad (9)$$

where E_{cell} is the full cell potential (V), and m is the mass of the produced ammonia (kg).

The cathodic energetic efficiency (EE_{ca}) for the electroreduction of NO_3^- toward NH_3 was calculated by the following equation:

$$\text{EE}_{\text{ca}} = E_{\text{eq},\text{cell}} \times \text{FE} / E_{\text{eq},\text{cell}} + \eta_{\text{cathode}} \quad (10)$$

where $E_{\text{eq},\text{cell}}$ is the thermodynamic equilibrium potential between anode and cathode reactions, and $E_{\text{eq},\text{cell}} = 1.23 + (-E_{\text{eq}})$; 1.23 V is the thermodynamic equilibrium potential for anode reaction (oxygen evolution reaction); E_{eq} is the thermodynamic equilibrium potential for cathode reaction (vs. RHE). $E_{\text{eq},\text{ammonia}} = 0.69 \text{ V}$, and the η_{cathode} is the cathode overpotential equal to the applied cathode potential (vs. RHE) minus the thermodynamic equilibrium potential.

3. Results and discussion

3.1. Morphology and crystallinity characterizations of catalysts

The Fe-N-BC catalyst was synthesized through a one-step pyrolysis

method (Fig. 1a). Scanning electron micrographs (Supporting Information, Fig. S1a, b) show the morphology changes from carbonized algal biomass (BC) to KOH-activated biochar (N-BC). The BC exhibited a relatively smooth surface, while N-BC possesses a porous structure with a higher specific surface area (Supporting Information, Fig. S2). This phenomenon is attributed to the biochar being etched by KOH during the heating process, then the gaseous products from the activation process further react with the carbon matrix [43]. The results above were expected to provide a large electrochemically active surface area (ECSA) and numerous active sites [42]. Compare to N-BC, no noticeable morphology changes could be observed after Fe-doping (Fe-N-BC) (Supporting Information, Fig. S1c). EDS mapping confirmed the uniform dispersion of Fe dopants in the biochar matrix (Fig. 1b-c). The dispersed individual Fe atoms also could be observed by using an aberration-corrected HAADF-STEM (Fig. 1e).

The X-ray diffractogram of Fe-N-BC indicated two broad diffraction peaks located at $22.58^\circ 2\theta$ and $44.05^\circ 2\theta$ ascribed to the (002) and (101) crystal plane of disordered carbons, respectively [44], while no peaks related to metallic Fe or other crystalline Fe species were presented (Supporting Information, Fig. S3a). Based on Bragg's law, the calculated interlayer spacing of Fe-N-BC is 0.391 nm , larger than that of graphite (0.335 nm), suggesting a poorly developed local order in the carbon matrix [45]. According to the Scherrer equation, the average length along the c direction (L_c) is 1.041 nm (Supporting Information, Eq. S1), which conforms to the characteristics of amorphous carbon [44]. Besides, two peaks presented at 1330 cm^{-1} and 1590 cm^{-1} from Raman spectra, which were corresponding to the disorder-induced D-band and ordered sp^2 -hybridized vibrational G-band with a I_D/I_G ratio of 1.31 (Supporting Information, Fig. S3b). Accordingly, the apparent average length along lateral ab direction (L_a) of potential graphitic carbon domains is calculated as 12.56 nm using Supporting Information Eq. S2 [46]. In addition, TEM image depicted the coexistence of disordered and graphitic carbons (Fig. 1d), which was consistent with XRD and Raman spectra results. With different Fe doping levels as well as different transition metal dopants, other control samples including commercially available graphite (Co and Cu) were also characterized and evaluated (Supporting Information, Fig. S4-S5).

3.2. Electrocatalytic NO_3RR performance

In this study, all the electrochemical NO_3RR were carried out at ambient conditions in a standard three-electrode H-type cell. The accumulated NH_3 , NO_3^- , and NO_2^- were quantified via ultraviolet-visible (UV-vis) spectrophotometry (Supporting Information, Part S3, Fig. S6). Typically, 100 mM of nitrate ($1400 \mu\text{g mL}^{-1}$ of NO_3^- -N) was contained in the electrolyte for standard electrochemical characterizations. As shown in the $I-V$ plot (Fig. 2a), Fe-N-BC presented distinct electrocatalytic behaviors compared with C and N-BC. Fe-N-BC reached a limiting current density of about 420 mA cm^{-2} at around -0.5 V , which is 11 times larger than other control samples. At a relatively lower potential of -0.22 V , Fe-N-BC obtained about 65% NH_3 FE and a maximum NH_3 FE of 87% at -0.42 V respectively, implying the facile NO_3RR kinetics on the Fe dopants (Fig. 2b). EE_{ca} reached 20.2% for Fe-N-BC, higher than that of N-BC (11.3%) and C (4.2%). Accordingly, high ammonia selectivity of 88% and ammonia generation rate at $16,449 \mu\text{g cm}^{-2} \text{ h}^{-1}$ of the Fe-N-BC could be achieved (Fig. 2c). As the overpotential further increases, NH_3 FE of Fe-N-BC decreases due to the HER competition (Supporting Information, Fig. S7). Ammonia FE decreased from 87% to 68% during the electrocatalytic NO_3RR process (Fig. 2d), which is attributed to the decreased nitrate concentration on the electrode surface. As shown in the $I-t$ plot (Supporting Information, Fig. S8), the apparent current density also declined distinctly, suggesting that the kinetically sluggish electrocatalytic HER by Fe-N-BC at -0.42 V . After 12 h of electrocatalytic reaction, NO_3^- and NO_2^- were both reduced below the WHO regulations for drinking water (NO_3^- -N $< 11.3 \mu\text{g mL}^{-1}$ and NO_2^- -N $< 0.9 \mu\text{g mL}^{-1}$; Fig. 2d).

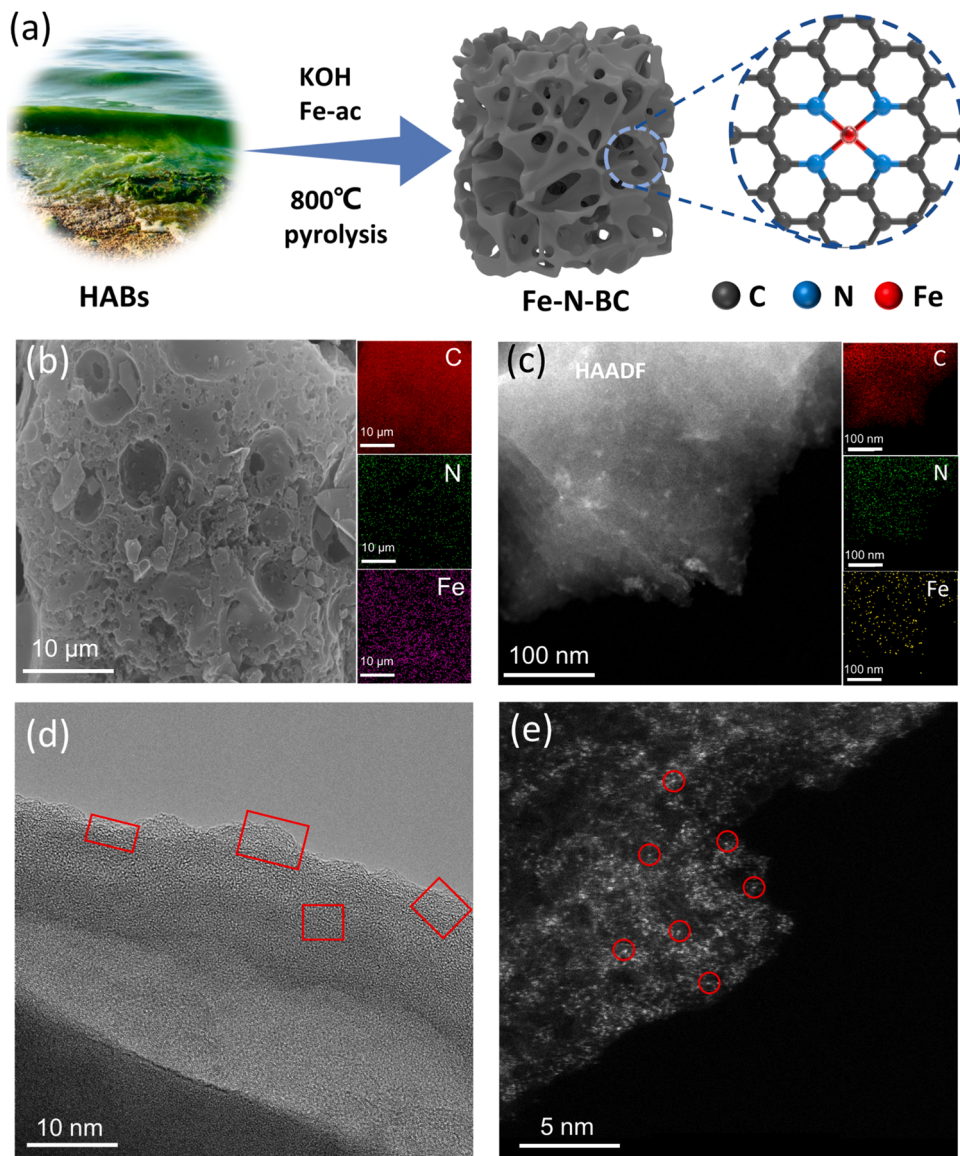


Fig. 1. (a) Schematic of Fe-N-BC synthesis process. (b) and (c) EDS mappings of Fe-N-BC. The scale bar is 10 μm and 100 nm, respectively. (d) TEM image and (e) Aberration-corrected HAADF-STEM image of Fe-N-BC (some single atoms are circled in red).

Isotope-labelled $^{15}\text{NO}_3^-$ electroreduction experiments and ^1H NMR analysis confirmed that all NH_3 products were generated by electrocatalytic NO_3^- RR rather than by any contaminations as nitrogen source from carbon matrix and N_2 (Fig. 2e). To compare the energy efficiency of NH_3 production at different cathode potentials, four energy efficiency indicators as NH_3 production rate, NH_3 selectivity, 1/EC for NH_3 production, and FE towards NH_3 were normalized to a Nightingale diagram (Fig. 2f). Seemingly, -0.42 V is optimal for electrochemical NO_3^- RR in light of its largest pie area, while the NH_3 production rate is more sensitive to applied potential than other elements owing to its significant changes.

Regarding the wide range of nitrate concentrations from various polluting sources [47–52], Fe-N-BC catalytic performance was also investigated at $100 \mu\text{g mL}^{-1}$, $700 \mu\text{g mL}^{-1}$, and $1400 \mu\text{g mL}^{-1}$ of NO_3^- -N. Expectedly, reaction rates of electrochemical NO_3^- RR decreased with lowering nitrate concentrations, as could be evidenced by decreased current density (Fig. 3a). Fe-N-BC not only obtained 87% NH_3 FE under higher NO_3^- -N concentration but also performed well under $100 \mu\text{g mL}^{-1}$ NO_3^- -N with an NH_3 FE over 80% (Fig. 3b). For $1400 \mu\text{g mL}^{-1}$, the denitrification capacity and ammonia production rate of the Fe-N-BC

catalyst achieved $19989 \pm 458 \mu\text{g h}^{-1} \text{ mg}_{\text{cat}}^{-1}$, NO_3^- -N and $20562 \pm 661 \mu\text{g h}^{-1} \text{ mg}_{\text{cat}}^{-1}$, respectively (Fig. 3c). From Fig. 3d, the NO_3^- RR performance of Fe-N-BC almost outperforms other reported catalysts with higher current density accompanied by higher NH_3 FE, and superior ammonia yield rate. Therefore, Fe-N-BC offers favorable potential for complete nitrate removal and nitrate conversion into ammonia in wastewater.

To evaluate the intrinsic electrocatalytic NO_3^- RR activities of catalysts, ECSA was obtained from electrochemical double-layer capacitance (C_{dl}) and used to normalize the current density (Supporting Information, Fig. S9). The ECSA of Fe-N-BC reached 1321, which is significantly larger than the other catalysts. Presented with a larger ECSA-normalized current density toward ammonia than other catalysts (Supporting Information, Fig. S10), the good performance of Fe-N-BC originates likely not only from its high ECSA but from a higher intrinsic NO_3^- RR activity [42].

3.3. Revealing the detailed structure of Fe-N-BC

The oxidation state and coordination environment of Fe were

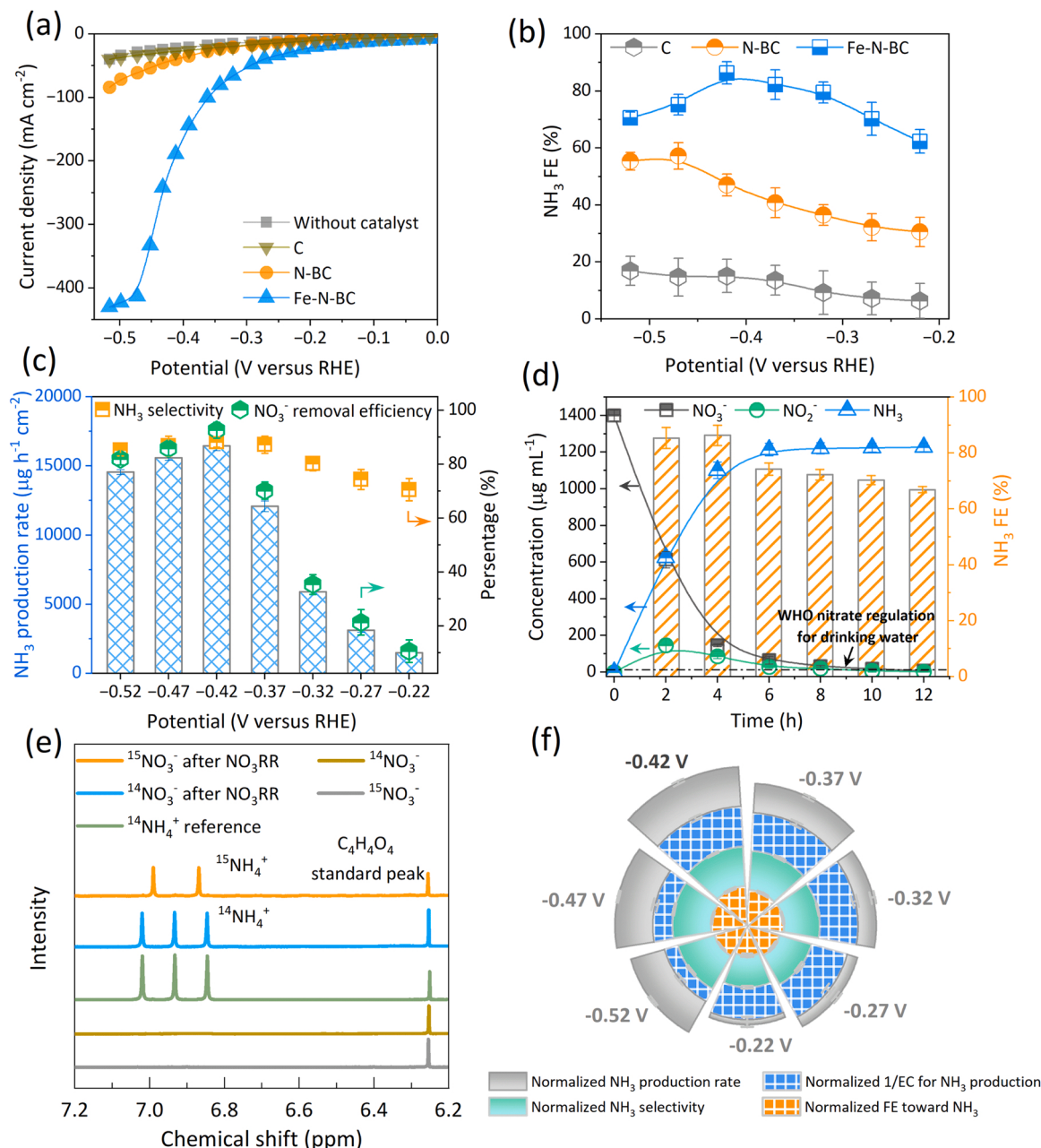


Fig. 2. (a) LSV curves and (b) the corresponding NH₃ FE of different catalysts at different potentials. (c) NO₃RR performance of Fe-N-BC at different potentials. (d) Complete nitrate removal using Fe-N-BC at -0.42 V versus RHE. After 12 h of electrolysis, only 4.82 μg L⁻¹ of NO₃-N and 0.51 μg L⁻¹ of NO₂-N remained. (e) ¹H NMR spectra before and after NO₃RR using ¹⁵NO₃ and ¹⁴NO₃ electrolytes. (f) Variations of normalized NH₃ production rate, 1/EC, NH₃ selectivity, and FE toward NH₃ under different potentials. Reaction conditions: in a 1 M KOH with 0.1 M KNO₃ electrolyte.

investigated to unravel the mechanism underlying Fe-N-BC high intrinsic activity. XPS survey spectra show the existence of evident C, O, and N peaks in Fe-N-BC except for weakly Fe peaks (Supporting Information, Fig. S3), as iron was less abundant in Fe-N-BC (ca. 1.2 mass% determined by ICP-OES). The high-resolution Fe 2p XPS spectrum also confirmed the absence of metallic iron in the Fe-N-BC, of which Fe (II) was the dominant iron species (Supporting Information, Fig. S11) [53]. The N 1 s spectrum of Fe-N-BC (Fig. 4a) confirms the presence of four types of N species, namely, pyridinic N (398.1 eV), Fe-N (398.7 eV), pyrrolic N (399.6 eV), and graphitic N (401.5 eV) [53]. A small up-shift peak assigned to the pyridinic N, which could be observed in the N 1 s spectra of Fe-N-BC related to the position in N-BC. Compared with N-BC, the proportion of pyridinic N was increased in Fe-N-BC. Herein, pyridinic N dopants in Fe-N-BC are primarily coordinated with the Fe atom,

while the ratio of graphitic N transformed from pyridinic N decreased during the annealing process [54].

XAES results further revealed the electronic properties of the Fe in Fe-N-BC and the coordination structures of the Fe dopants. XANES spectrum of the Fe-N-BC depicted that the Fe K-pre-edge was located between the Fe-foil and Fe₂O₃, suggesting the positive state of Fe in Fe-N-BC (Fig. 4b) [53]. The Fourier transform-EXAFS (FT-EXAFS) curve of Fe-N-BC (Fig. 4c) presented one central peak at about 1.5 Å, ascribing to the Fe-N first coordination shell [55]. No prominent peaks of Fe-Fe (2.2 Å) and Fe-O (1.4 Å) are observed, demonstrating that the Fe dopants were atomically dispersed in Fe-N-BC. To achieve a high resolution in both k and R spaces, the wavelet transform was carried out for further EXAFS analysis (Fig. 4d) [56]. In comparison with the wavelet transform contour plots of Fe-foil and Fe₂O₃, the Fe-N-BC exhibits only one

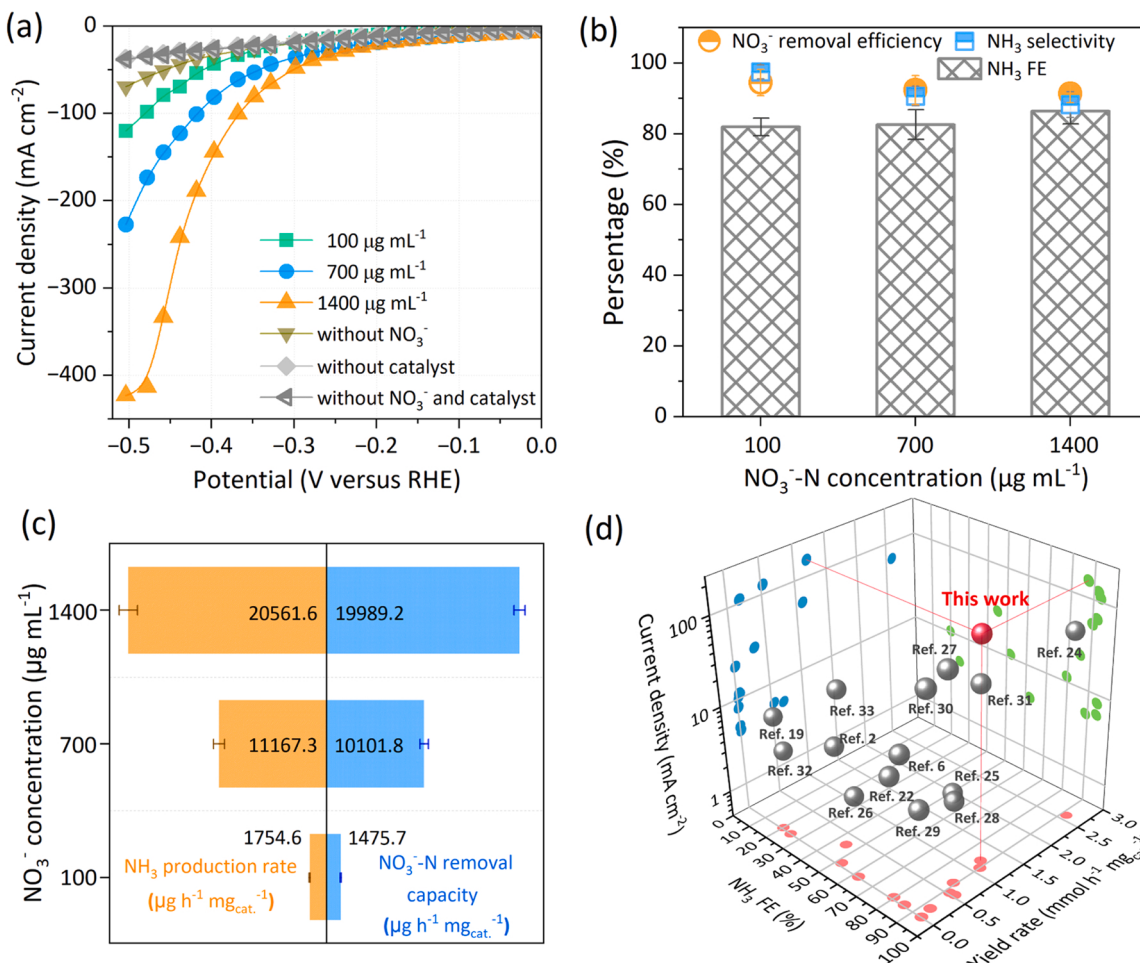


Fig. 3. (a) LSV curves of Fe-N-BC upon different NO_3^- concentrations. (b) NO_3 RR performance of Fe-N-BC in different NO_3^- concentrations electrolyte. (c) Nitrate removal capacities and NH_3 production rate of Fe-N-BC. Reaction conditions: 4 h of electrolysis at -0.42 V versus RHE. (d) Comparison of the reported NO_3 RR performance.

intensity maximum at around 4.1 \AA^{-1} , suggesting that the coordination of Fe atoms in Fe-N-BC is different with Fe-foil and Fe_2O_3 . Furthermore, in Fig. 4e, the EXAFS fitting structural parameters indicate that the Fe coordination environment in Fe-N-BC be Fe-N_4 structure, as presented in Supporting Information, Fig. S12 (optimized by DFT). Therefore, the Fe dopants were coordinated with nitrogen and highly dispersed as isolated atoms in the carbon substrate.

3.4. Density functional theory calculations

To understand how Fe-N-BC possesses high NH_3 FE over other referenced catalysts, DFT calculations were conducted to obtain the Gibbs free energy for NO_3 RR and HER process on various catalyst surfaces (Supporting Information, Part S5). In Fig. 5a, the potential determining step (PDS) for NO_3 RR is contributed by the process of $^*e - N + O + 2 \rightarrow *NO + 2$ on the surface of Fe-N-BC and N-BC, and the process of $^*e - NH + O + \rightarrow *NH_2 +$ on the surface of C as well. Notably, Fe-N-BC exhibits the lowest Gibbs energy barrier of 0.474 eV in comparison to 1.70 eV and 1.99 eV for N-BC and C, respectively. It was demonstrated that NO_3 RR can occur most preferentially on the Fe-N-BC surface. As for HER, free energies for *H_2O were calculated as -0.73 eV, which is smaller than the energies for $^*\text{NO}_3$ (-3.05 eV). Therefore, it was more favorable for NO_3^- adsorption on Fe-N-BC surface at pH 14 (Fig. 5b). Moreover, the PDS for HER on Fe-N-BC surface is $^*e - O + \rightarrow *H +$, whereas the energy barrier is 0.42 eV. Due to the similar energy barrier for NO_3 RR and HER on Fe-N-BC surface, as well as

the higher adsorption energy for NO_3^- than H_2O , HER activity might be inhibited. The differential charge density was used to investigate the interactions between the catalysts and NO_3^- , it can be found that the electrons appreciably transferred from Fe to NO_3^- on the Fe-N-BC surface (Fig. 5c), which would further facilitate the NO_3 RR process [57]. Moreover, the weak interaction between NO_3^- and N-BC surface could explain the slow kinetics of NO_3 RR on the N-BC surface. To further understand the electronic structures, the partial density of states (PDOS) for the adsorption behavior of $^*\text{NO}_3$ on Fe-N-BC and N-BC were calculated. As shown in Fig. 5d, 3d orbitals of the Fe single atoms interacted strongly with the 2p orbital of the O atoms, leading to the transfer of electrons from the occupied Fe 3d orbital to the lowest unoccupied molecular orbital of the NO_3^- molecules, which promoted N = O bond cleavage [58]. Overall, the DFT calculation further uncovers why Fe-N-BC possesses high ammonia FE and higher intrinsic NO_3 RR activity.

3.5. Ammonia downstream product conversion and catalyst stability

On the premise that the Fe-N-BC obtains better NO_3 RR performance, conversion from ammonia to downstream products was also explored. In Supporting Information, Fig. S13, using the air stripping method to separate the NH_3 from the electrolyte, the ammonia vapor was trapped in an HCl solution to form NH_4Cl . At first, the electrochemical NO_3 RR was operated for 8 batches using Fe-N-BC in an H cell and the current density was kept at 150 mA cm^{-2} (Fig. 6a). Over 80% ammonia FE was

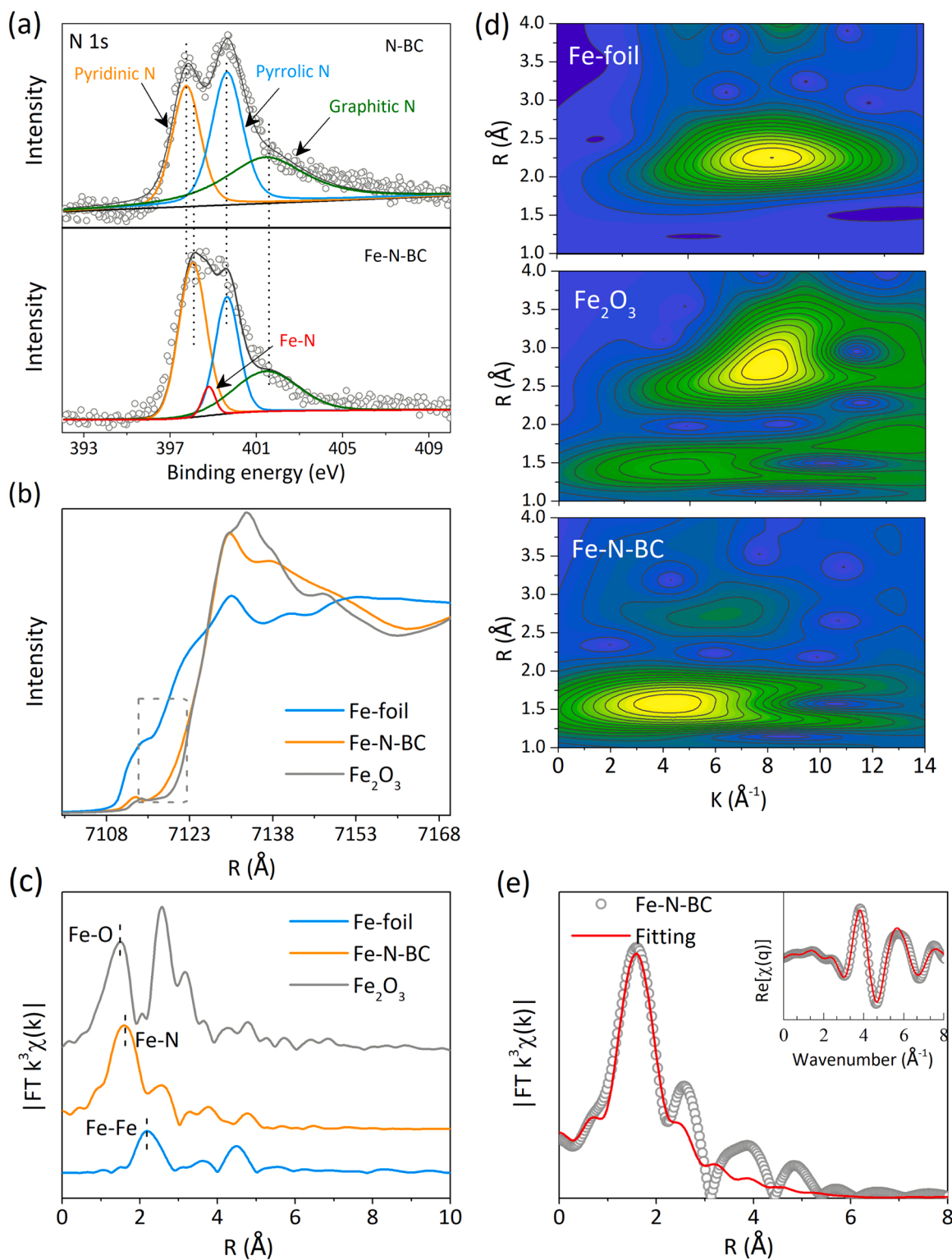


Fig. 4. (a) N 1 s XPS spectra of N-BC and Fe-N-BC. (b) Fe K-edge XANES spectra, (c) Fe K-edge FT-EXAFS, and (d) WT-EXAFS spectra of Fe-N-BC, Fe_2O_3 , and Fe foil. (e) Corresponding EXAFS fitting curves for Fe-N-BC.

maintained even at the 8th batch, while the potential only decreased by 0.22 V at the plateau potential. Physicochemical characterization demonstrated that the morphology and structure of Fe-N-BC were not significantly altered after electrocatalytic NO_3RR (Supporting Information, Fig. S14). Also, the average iron concentration in the electrolyte after 8 batches (over 40 h) NO_3RR reached only $3.6 \mu\text{g L}^{-1}$, the mass of Fe element dissolution in the electrolyte accounts for $\sim 14\%$ ($1.4 \mu\text{g}$) of

the total Fe mass. (Supporting Information, Fig. S15). Then, the electrolyte was kept for subsequent ammonia separation.

Fig. 6b shows the mass flows and species distributions regarding the NO_3RR and downstream products. After NO_3RR , the nitrate removal efficiency attained over 85%, whereas 86.4% of which was converted to ammonia conversion. After 8 h of air-stripped operation, the conversion rate from total generated NH_3 to NH_4Cl reached 95%, as could be

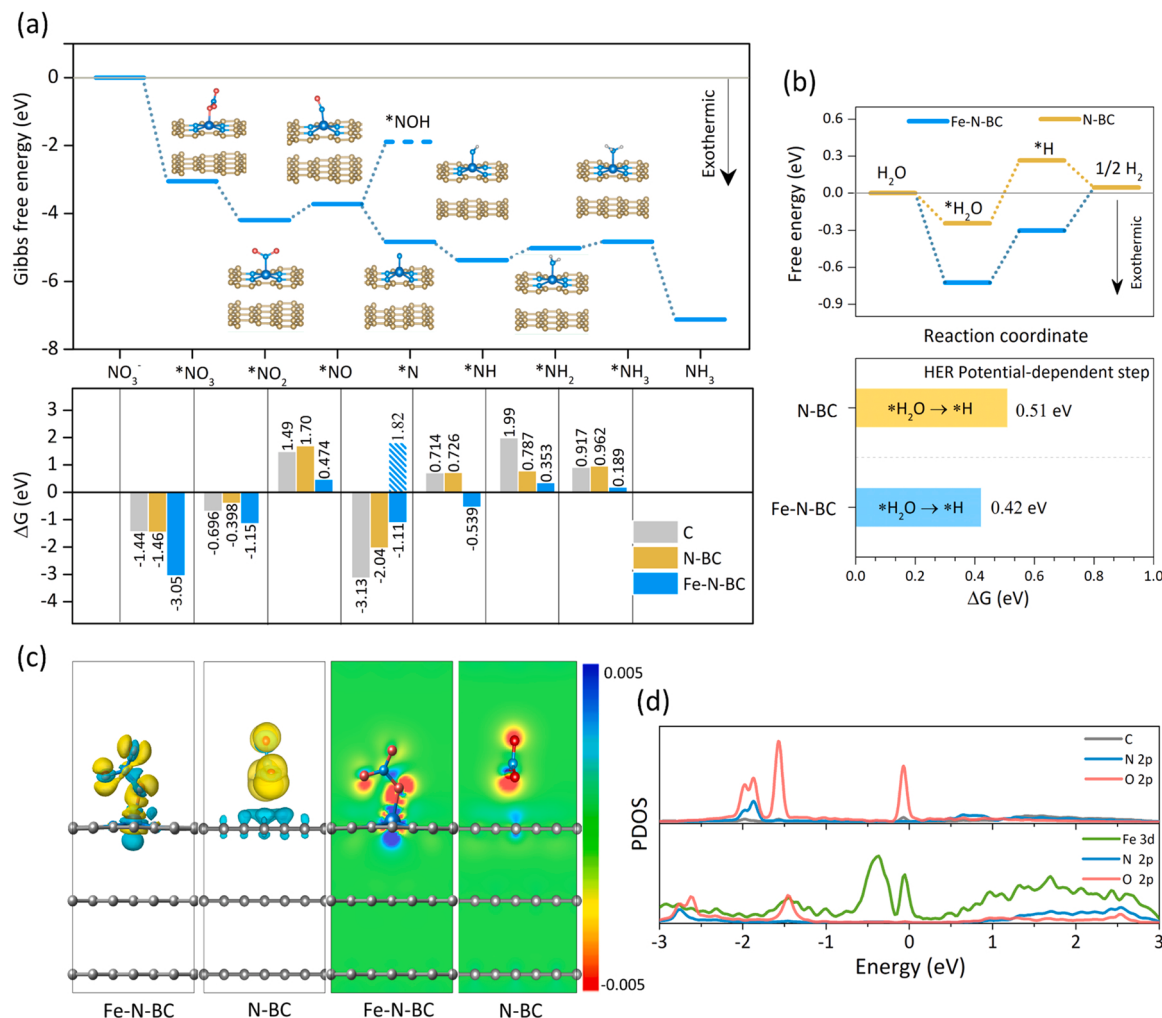


Fig. 5. (a) Gibbs free energy diagram of NO_3 RR occurring on Fe-N-BC surface (upper) and the change in Gibbs free energy between the steps on different surfaces (lower). (b) The reaction energies of H_2 formation and PDS energy barriers over N-BC and Fe-N-BC. (c) Differential charge density plot of NO_3 adsorbed on the surface. (d) PDOS of Fe-N-BC and N-BC with NO_3^- adsorbed.

confirmed by the corresponding X-ray diffractogram consistent with PDF 34-0710 (cubic ammonium chloride; Fig. 6c) [42]. Additionally, preliminary experiments to probe the possibility of the electrocatalytic C-N coupling reaction were performed using Fe-N-BC (Supporting Information, Part S6, Fig. S16). It was found that the yield rate of urea reached $120 \mu\text{g h}^{-1} \text{cm}^{-2}$, while corresponding FE measured at -0.8 V versus RHE reached 1.2% (Fig. 6d).

In summary, Fe-N-BC shows decent stability for electrochemical NO_3 RR, and the full process of converting nitrate into ammonia downstream products could also be expected.

3.6. Potential capability of carbon emission reduction

This recycling and upcycling process takes HABs biomass from biomass wastes grave to a green catalysts cradle via a win-win strategy to create a cost-effective and eco-friendly NO_3 RR as indicated by Fig. 6e. Supposedly, about 51,000 tons of carbon emissions could be reduced annually by carbonizing the Taihu HABs to biochar (Supporting Information, Eq. S15), which equals the sum of the per-capita carbon dioxide emissions of more than 6,000 people in China in 2021 (8.4 tons per capita carbon dioxide emissions) or Germany in 2020 (7.7 tons per capita carbon dioxide emissions) [59,60]. Currently, 2.8 tons of CO_2 emissions are accompanied per ton of NH_3 [61]. It can be envisioned that the carbonized Taihu HABs, used as catalysts for electrochemical NO_3 RR, could contribute to reducing CO_2 emissions by about 146,000,

000 tons per year (Supporting Information, Eq. S16). Combined with the appealing performance of Fe-N-BC for green ammonia synthesis, carbon neutrality would be promoted.

4. Conclusion

In summary, we have presented a facile strategy to recycle and upcycle HABs to prepare Fe atom dispersed carbon-based catalyst for NO_3 RR. By taking advantage of the large electrochemical surface area and high intrinsic activity of Fe-N₄ sites, the Fe-N-BC delivers an approximate industrial current density of 150 mA cm^{-2} for NO_3 RR with a maximum FE of 87.3% and NH_3 yield rate reached $16449 \mu\text{g h}^{-1} \text{cm}^{-2}$ ($1.2 \text{ mmol h}^{-1} \text{mg}_{\text{cat}}^{-1}$). Mechanistic studies reveal that Fe single atom site in Fe-N-BC reduces the energy barriers of the NO_3 -to- NH_3 pathway. The conversion rate of ammonia into its downstream product of NH_4Cl was achieved at 95.0% with the air stripping process. Consequently, this work provides a new horizon for HABs utilization. In the future, assembling this catalyst with flow-cell to electrocatalytic C-N coupling reactions for more practical implementations could be further investigated.

CRediT authorship contribution statement

He Wang: Conceptualization, Methodology, Data curation, Writing – original draft. **Shuaishuai Man:** Methodology, Validation, Formal

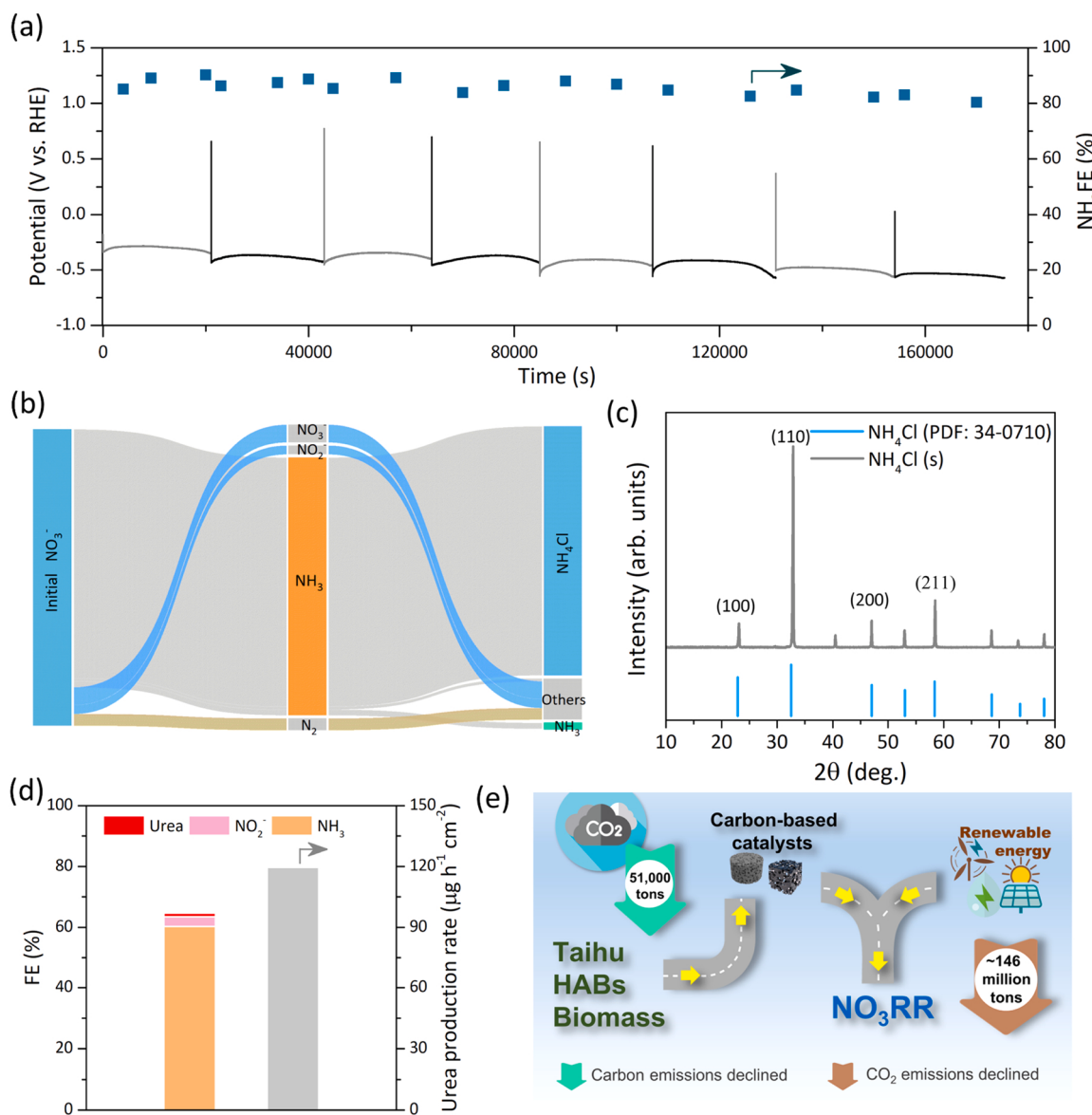


Fig. 6. (a) Testing of chronopotentiometry stability for Fe-N-BC during eight consecutive cycling NO_3 RR processes at 150 mA cm^{-2} . (b) Distributions of nitrogen species within different operation stages. (c) XRD analysis result of obtained NH_4Cl (s) products. (d) Urea production rate and FE of the primary C-N coupling reaction. (e) Schematic diagram of HABs-derived carbon-based catalysts for electrochemical NO_3 RR, aimed to reduce carbon emissions.

analysis, Writing – original draft. **Han Wang**: Investigation, Data curation. **Volker Presser**: Supervision, Writing – review & editing. **Qun Yan**: Resources, Project administration, Funding acquisition, Supervision, Writing – original draft, Writing – review & editing. **Yong Zhang**: Supervision.

Declaration of Competing Interest

The authors declare that they have no known competing financial interests or personal relationships that could have appeared to influence the work reported in this paper.

Data Availability

No data was used for the research described in the article.

Acknowledgements

This research was financially supported by the National Key

Research and Development Program of China (Award number: 2017YFE9133400), National Natural Science Foundation of China (Award number: 51908245), Taizhou Science and Technology Support Program of Jiangsu Province, China (Award number: TG202258), and the Pre-research Fund of Jiangsu Collaborative Innovation Center of Technology and Material of Water Treatment (Award number: XTCXSZ2020-3). Shuaishuai Man acknowledges funding from the Chinese Scholarship Council (CSC) via award number 202106050060.

Appendix A. Supporting information

Supplementary data associated with this article can be found in the online version at doi:10.1016/j.apcatb.2023.122778.

References

- [1] J.W.R. Department, (http://jsslt.jiangsu.gov.cn/art/2021/12/9/art_43066_10187067.html), 2021.

- [2] Y. Xue, Q. Yu, Q. Ma, Y. Chen, C. Zhang, W. Teng, J. Fan, W.X. Zhang, Electrocatalytic hydrogenation boosts reduction of nitrate to ammonia over single-atom Cu with Cu(I)-N(3)C(1) sites, *Environ. Sci. Technol.* 56 (2022) 14797–14807.
- [3] J. Yang, T. Zhao, X. Cui, M. Peng, X. Wang, H. Mao, M. Cui, New insights into the carbon neutrality of microalgae from culture to utilization: a critical review on the algae-based solid biofuels, *Biomass Bioenerg.* 166 (2022), 106599.
- [4] Q. Cao, C. Wang, D. Tang, X. Zhang, P. Wu, Y. Zhang, H. Liu, Z. Zheng, Enhanced elemental mercury removal in coal-fired flue gas by modified algal waste-derived biochar: performance and mechanism, *J. Environ. Manag.* 325 (2022), 116427.
- [5] P.H. van Langevelde, I. Katsounaros, M.T.M. Koper, Electrocatalytic nitrate reduction for sustainable ammonia production, *Joule* 5 (2021) 290–294.
- [6] S. Zhang, M. Li, J. Li, Q. Song, X. Liu, High-ammonia selective metal-organic framework-derived Co-doped Fe/Fe₂O₃ catalysts for electrochemical nitrate reduction, *Proc. Natl. Acad. Sci.* 119 (2022), e2115504119.
- [7] J.M. McEnaney, S.J. Blair, A.C. Nielander, J.A. Schwalbe, D.M. Koshy, M. Cargnelli, T.F. Jaramillo, Electrolyte engineering for efficient electrochemical nitrate reduction to ammonia on a titanium electrode, *ACS Sustain. Chem. Eng.* 8 (2020) 2672–2681.
- [8] V. Rosca, M. Duca, M.Td Groot, M.T.M. Koper, Nitrogen cycle electrocatalysis, *Chem. Rev.* 109 (2009) 2209–2244.
- [9] J. Guo, P. Chen, Catalyst: NH₃ as an energy carrier, *Chem* 3 (2017) 709–712.
- [10] Y. Wang, C. Wang, M. Li, Y. Yu, B. Zhang, Nitrate electroreduction: mechanism insight, in situ characterization, performance evaluation, and challenges, *Chem. Soc. Rev.* 50 (2021) 6720–6733.
- [11] R. Lan, J.T.S. Irvine, S. Tao, Ammonia and related chemicals as potential indirect hydrogen storage materials, *Int. J. Hydrog. Energ.* 37 (2012) 1482–1494.
- [12] S. Mallapatty, How China could be carbon neutral by mid-century, *Nature* 586 (2020) 482–483.
- [13] Z. Yan, J.L. Hitt, J.A. Turner, T.E. Mallouk, Renewable electricity storage using electrolysis, *Proc. Natl. Acad. Sci.* 117 (2020) 12558–12563.
- [14] X. Cui, C. Tang, Q. Zhang, A review of electrocatalytic reduction of dinitrogen to ammonia under ambient conditions, *Adv. Energ. Mater.* 8 (2018), 1800369.
- [15] J. Wang, T. Feng, J. Chen, V. Ramalingam, Z. Li, D.M. Kabatamu, J.-H. He, X. Fang, Electrocatalytic nitrate/nitrite reduction to ammonia synthesis using metal nanocatalysts and bio-inspired metalloenzymes, *Nano Energ.* 86 (2021), 106088.
- [16] J. Li, G. Zhan, J. Yang, F. Quan, C. Mao, Y. Liu, B. Wang, F. Lei, L. Li, A.W.M. Chan, L. Xu, Y. Shi, Y. Du, W. Hao, P.K. Wong, J. Wang, S.X. Dou, L. Zhang, J.C. Yu, Efficient ammonia electrosynthesis from nitrate on strained ruthenium nanoclusters, *J. Am. Chem. Soc.* 142 (2020) 7036–7046.
- [17] G.E. Dima, A.C.A. de Vooy, M.T.M. Koper, Electrocatalytic reduction of nitrate at low concentration on coinage and transition-metal electrodes in acid solutions, *J. Electroanal. Chem.* 554–555 (2003) 15–23.
- [18] Y. Wang, A. Xu, Z. Wang, L. Huang, J. Li, F. Li, J. Wicks, M. Luo, D.H. Nam, C. S. Tan, Y. Ding, J. Wu, Y. Lum, C.T. Dinh, D. Sinton, G. Zheng, E.H. Sargent, Enhanced nitrate-to-ammonia activity on copper-nickel alloys via tuning of intermediate adsorption, *J. Am. Chem. Soc.* 142 (2020) 5702–5708.
- [19] Y. Li, S. Xiao, X. Li, C. Chang, M. Xie, J. Xu, Z. Yang, A robust metal-free electrocatalyst for nitrate reduction reaction to synthesize ammonia, *Mater. Today Phys.* 19 (2021), 100431.
- [20] R.D. Milton, S.D. Minteer, Enzymatic bioelectrosynthetic ammonia production: Recent electrochemistry of nitrogenase, nitrate reductase, and nitrite reductase, *Chempluschem* 82 (2017) 513–521.
- [21] X. Liang, H. Zhu, X. Yang, S. Xue, Z. Liang, X. Ren, A. Liu, G. Wu, Recent advances in designing efficient electrocatalysts for electrochemical nitrate reduction to ammonia, *Small Struct.* (2022), 2200202.
- [22] Y. Liu, B. Deng, K. Li, H. Wang, Y. Sun, F. Dong, Metal-organic framework derived carbon-supported bimetallic copper-nickel alloy electrocatalysts for highly selective nitrate reduction to ammonia, *J. Colloid Interface Sci.* 614 (2022) 405–414.
- [23] S. Xu, Y. Shi, Z. Wen, X. Liu, Y. Zhu, G. Liu, H. Gao, L. Sun, F. Li, Polystyrene spheres-templated mesoporous carbonous frameworks implanted with cobalt nanoparticles for highly efficient electrochemical nitrate reduction to ammonia, *Appl. Catal. B: Environ.* 323 (2023), 122192.
- [24] W.-D. Zhang, H. Dong, L. Zhou, H. Xu, H.-R. Wang, X. Yan, Y. Jiang, J. Zhang, Z.-G. Gu, Fe single-atom catalysts with pre-organized coordination structure for efficient electrochemical nitrate reduction to ammonia, *Appl. Catal. B: Environ.* 317 (2022), 121750.
- [25] X. Zhang, G. Ma, L. Shui, G. Zhou, X. Wang, Ni₃N nanoparticles on porous nitrogen-doped carbon nanorods for nitrate electroreduction, *Chem. Eng. J.* 430 (2022), 132666.
- [26] Z. Wang, C. Sun, X. Bai, Z. Wang, X. Yu, X. Tong, Z. Wang, H. Zhang, H. Pang, L. Zhou, W. Wu, Y. Liang, A. Khosla, Z. Zhao, Facile synthesis of carbon nanobelts decorated with Cu and Pd for nitrate electroreduction to ammonia, *ACS Appl. Mater. Interf.* 14 (2022) 30969–30978.
- [27] Q. Chen, J. Liang, L. Yue, Y. Luo, Q. Liu, N. Li, A.A. Alshehri, T. Li, H. Guo, X. Sun, CoO nanoparticle decorated N-doped carbon nanotubes: a high-efficiency catalyst for nitrate reduction to ammonia, *Chem. Commun.* 58 (2022) 5901–5904.
- [28] H. Chen, C. Zhang, L. Sheng, M. Wang, W. Fu, S. Gao, Z. Zhang, S. Chen, R. Si, L. Wang, B. Yang, Copper single-atom catalyst as a high-performance electrocatalyst for nitrate-ammonium conversion, *J. Hazard. Mater.* 434 (2022), 128892.
- [29] E. Murphy, Y. Liu, I. Matanovic, S. Guo, P. Tieu, Y. Huang, A. Ly, S. Das, I. Zenyuk, X. Pan, E. Spoerke, P. Atanassov, Highly durable and selective Fe- and Mo-based atomically dispersed electrocatalysts for nitrate reduction to ammonia via distinct and synergized NO₂ Pathways, *ACS Catal.* 12 (2022) 6651–6662.
- [30] T. Xie, X. Li, J. Li, J. Chen, S. Sun, Y. Luo, Q. Liu, D. Zhao, C. Xu, L. Xie, X. Sun, Co nanoparticles decorated corncob-derived biomass carbon as an efficient electrocatalyst for nitrate reduction to ammonia, *Inorg. Chem.* 61 (2022) 14195–14200.
- [31] Q. Chen, J. Liang, Q. Liu, K. Dong, L. Yue, P. Wei, Y. Luo, Q. Liu, N. Li, B. Tang, A. A. Alshehri, M.S. Hamdy, Z. Jiang, X. Sun, Co nanoparticle-decorated pomelo-peel-derived carbon enabled high-efficiency electrocatalytic nitrate reduction to ammonia, *Chem. Commun.* 58 (2022) 4259–4262.
- [32] Z. Chen, J. Chen, G. Barcaro, T.M. Budnyak, A. Rokicińska, R. Dronkowski, S. Budnyk, P. Kuśtrowski, S. Monti, A. Slabon, Reaction pathways on N-substituted carbon catalysts during the electrochemical reduction of nitrate to ammonia, *Catal. Sci. Technol.* 12 (2022) 3582–3593.
- [33] X. Li, Y. Gu, S. Wu, S. Chen, X. Quan, H. Yu, Selective reduction of nitrate to ammonium over charcoal electrode derived from natural wood, *Chemosphere* 285 (2021), 131501.
- [34] Y. Shang, X. Xu, B. Gao, S. Wang, X. Duan, Single-atom catalysis in advanced oxidation processes for environmental remediation, *Chem. Soc. Rev.* 50 (2021) 5281–5322.
- [35] X. Wang, J. Du, Q. Zhang, L. Gu, L. Cao, H.-P. Liang, In situ synthesis of sustainable highly efficient single iron atoms anchored on nitrogen doped carbon derived from renewable biomass, *Carbon* 157 (2020) 614–621.
- [36] L. Peng, X. Duan, Y. Shang, B. Gao, X. Xu, Engineered carbon supported single iron atom sites and iron clusters from Fe-rich Enteromorpha for Fenton-like reactions via nonradical pathways, *Appl. Catal. B: Environ.* 287 (2021), 119963.
- [37] H. Wang, H. Wang, H. Zhao, Q. Yan, Adsorption and Fenton-like removal of chelated nickel from Zn-Ni alloy electroplating wastewater using activated biochar composite derived from Taihu blue algae, *Chem. Eng. J.* 379 (2020), 122372.
- [38] H. Wang, H. Wang, G. Liu, Q. Yan, In-situ pyrolysis of Taihu blue algae biomass as appealing porous carbon adsorbent for CO₂ capture: Role of the intrinsic N, *Sci. Total. Environ.* 771 (2021), 145424.
- [39] H. Wang, H. Wang, Q. Yan, Peroxymonosulfate activation by algal carbocatalyst for organic dye oxidation: Insights into experimental and theoretical, *Sci. Total. Environ.* 816 (2022), 151611.
- [40] Y. Cao, S. Mao, M. Li, Y. Chen, Y. Wang, Metal/porous carbon composites for heterogeneouscatalysis: old catalysts with improved performance promoted by N-doping, *ACS Catal.* 7 (2017) 8090–8112.
- [41] B. Ravel, M. Newville, Athena, artemis, hephaestus: data analysis for X-ray absorption spectroscopy using IFEFFIT, *J. Synchrotron Radiat.* 12 (2005) 537–541.
- [42] F.Y. Chen, Z.Y. Wu, S. Gupta, D.J. Rivera, S.V. Lambeets, S. Pecaut, J.Y.T. Kim, P. Zhu, Y.Z. Finfrock, D.M. Meira, G. King, G. Gao, W. Xu, D.A. Cullen, H. Zhou, Y. Han, D.E. Perea, C.L. Muñich, H. Wang, Efficient conversion of low-concentration nitrate sources into ammonia on a Ru-dispersed Cu nanowire electrocatalyst, *Nat. Nanotechnol.* 17 (2022) 759–767.
- [43] J. Wang, S. Kaskel, KOH activation of carbon-based materials for energy storage, *J. Mater. Chem. C* 22 (2012) 23710.
- [44] J. Han, I. Johnson, Z. Liu, A. Kudo, M. Chen, Effect of local atomic structure on sodium ion storage in hard amorphous carbon, *Nano Lett.* 21 (2021) 6504–6510.
- [45] Y. Qi, Y. Lu, F. Ding, Q. Zhang, H. Li, X. Huang, L. Chen, Y.S. Hu, Slope-dominated carbon anode with high specific capacity and superior rate capability for high safety Na-ion batteries, *Angew. Chem. Int. Ed.* 58 (2019) 4361–4365.
- [46] L. Xiao, H. Lu, Y. Fang, M.L. Sushko, Y. Cao, X. Ai, H. Yang, J. Liu, Low-defect and low-porosity hard carbon with high coulombic efficiency and high capacity for practical sodium ion battery anode, *Adv. Energ. Mater.* 8 (2018), 1703238.
- [47] T.T.P. Nguyen, B.K.D. Do, N.N. Bui, M.A. Pham, T.V. Nguyen, Selectiveness of copper and polypyrrole modified copper electrodes for nitrate electroreduction: a comparative study and application in ground water, *ECS Trans.* 53 (2013) 41–52.
- [48] S. Garcia-Segura, M. Lanzarini-Lopes, K. Hristovski, P. Westerhoff, Electrocatalytic reduction of nitrate: Fundamentals to full-scale water treatment applications, *Appl. Catal. B: Environ.* 236 (2018) 546–568.
- [49] L. Su, K. Li, H. Zhang, M. Fan, D. Ying, T. Sun, Y. Wang, J. Jia, Electrochemical nitrate reduction by using a novel Co₃O₄/Ti cathode, *Water Res.* 120 (2017) 1–11.
- [50] P.M. Biradar, P.B. Dhamole, R.R. Nair, S.B. Roy, S.K. Satpati, S.F. D'Souza, S. Lele, A.B. Pandit, Long-term stability of biological denitrification process for high strength nitrate removal from wastewater of uranium industry, *Environ. Prog.* 27 (2008) 365–372.
- [51] R. Liao, K. Shen, A.M. Li, P. Shi, Y. Li, Q. Shi, Z. Wang, High-nitrate wastewater treatment in an expanded granular sludge bed reactor and microbial diversity using 454 pyrosequencing analysis, *Bioresour. Technol.* 134 (2013) 190–197.
- [52] T. Inaba, T. Goto, T. Aoyagi, T. Hori, K. Aoki, Y. Sato, N. Ono, T. Furukata, H. Habe, S. Ogino, A. Ogata, Biological treatment of ironworks wastewater with high-concentration nitrate using a nitrogen gas aerated anaerobic membrane bioreactor, *Chem. Eng. J.* 450 (2022), 138366.
- [53] Y. Zhou, X. Tao, G. Chen, R. Lu, D. Wang, M.X. Chen, E. Jin, J. Yang, H.W. Liang, Y. Zhao, X. Feng, A. Narita, K. Mullen, Multilayer stabilization for fabricating high-loading single-atom catalysts, *Nat. Commun.* 11 (2020) 5892.
- [54] Y. Shang, X. Liu, Y. Li, Y. Gao, B. Gao, X. Xu, Q. Yue, Boosting fenton-like reaction by reconstructed single Fe atom catalyst for oxidizing organics: Synergistic effect of conjugated π-π sp² structured carbon and isolated Fe-N₄ sites, *Chem. Eng. J.* 446 (2022), 137120.
- [55] L. Zhao, Y. Zhang, L.B. Huang, X.Z. Liu, Q.H. Zhang, C. He, Z.Y. Wu, L.J. Zhang, J. Wu, W. Yang, L. Gu, J.S. Hu, L.J. Wan, Cascade anchoring strategy for general mass production of high-loading single-atomic metal-nitrogen catalysts, *Nat. Commun.* 10 (2019) 1278.
- [56] Z. Xia, H. Zhang, K. Shen, Y. Qu, Z. Jiang, Wavelet analysis of extended X-ray absorption fine structure data: theory, application, *Phys. B: Condens. Matter* 542 (2018) 12–19.

- [57] Y. Qi, Y. Zhang, L. Yang, Y. Zhao, Y. Zhu, H. Jiang, C. Li, Insights into the activity of nickel boride/nickel heterostructures for efficient methanol electrooxidation, *Nat. Commun.* 13 (2022) 4602.
- [58] H. Wei, K. Huang, D. Wang, R. Zhang, B. Ge, J. Ma, B. Wen, S. Zhang, Q. Li, M. Lei, C. Zhang, J. Irawan, L.-M. Liu, H. Wu, Iced photochemical reduction to synthesize atomically dispersed metals by suppressing nanocrystal growth, *Nat. Commun.* 8 (2017) 1490.
- [59] B. Aslam, J. Hu, S. Shahab, A. Ahmad, M. Saleem, S.S.A. Shah, M.S. Javed, M. K. Aslam, S. Hussain, M. Hassan, The nexus of industrialization, GDP per capita and CO₂ emission in China, *Environ. Technol. Inno.* 23 (2021), 101674.
- [60] G.F.S. Office, (https://www.destatis.de/EN/Themes/Countries-Regions/International-Statistics/Data-Topic/Tables/BasicData_CO2.html), Key table Carbon dioxide emissions per capita, German Federal Statistical Office, 2022.
- [61] L.K. Boerner, Industrial ammonia production emits more CO₂ than any other chemical-making reaction, *Chem. Eng. News*, 2019.